Photocatalytic, corrosion protection and adhesion properties of acrylic nanocomposite coating containing silane treated nano zinc oxide

A combined experimental and simulation study

Javadi, E.; Ghaffari, M.; Bahlakeh, Ghasem; Taheri, Peyman

DOI
10.1016/j.porgcoat.2019.06.039

Publication date
2019

Document Version
Accepted author manuscript

Published in
Progress in Organic Coatings

Citation (APA)
Javadi, E., Ghaffari, M., Bahlakeh, G., & Taheri, P. (2019). Photocatalytic, corrosion protection and adhesion properties of acrylic nanocomposite coating containing silane treated nano zinc oxide: A combined experimental and simulation study. *Progress in Organic Coatings*, *135*, 496-509. https://doi.org/10.1016/j.porgcoat.2019.06.039

Manuscript Details

Manuscript number	POC_2019_683
Title	Photocatalytic, corrosion protection and adhesion properties of acrylic nanocomposite coating containing silane treated nano zinc oxide: a combined experimental and simulation study
Short title	Photocatalytic, corrosion protection and adhesion properties of acrylic nanocomposite
Article type	Research Paper

Abstract

The influence of silane treated nano zinc oxide (nZnO) on the protection, photocatalytic properties and interfacial interactions in acrylic/carbon steel systems was investigated. For this purpose, nZnO particles have been synthesized using microwave irradiation method. The morphology of synthesized zinc oxide nanoparticles was studied by scanning electron microscopy (SEM). The nZnO were treated by 3(2-amino ethyl amino) propyl trimethoxysilane. Fourier transforms infrared spectroscopy (FTIR) and thermogravimetry (TGA) techniques have been used to prove success of nZnO surface treatment. In the next step, nanocomposites were prepared and coated on carbon steel by dip-coating method. Corrosion resistances of coatings were evaluated by electrochemical impedance spectroscopy (EIS). Field emission scanning electron microscopy (FE-SEM) has been carried out to study morphology of cross section of films. Moreover, to study the hydrophillicity and photocatalytic properties of coating surface, contact angle of the nanocomposites coating surface have been measured. Finally interfacial adhesion and their mechanisms have been studied by molecular dynamics (MD) and first principle quantum mechanics (QM) simulation method.

Keywords	Self-cleaning; Zinc oxide; Simulation; nanocomposite; surface treatment; acrylic

Corresponding Author	Mehdi Ghaffari
Order of Authors	Ehsan Javadi, Mehdi Ghaffari, Ghasem Bahlakeh, Peyman Taheri

Suggested reviewers	Reza Naderi, Mohammad Reza Saeb, Dawei Zhang

Submission Files Included in this PDF

File Name [File Type]

Cover letter.docx [Cover Letter]

Manuscript.docx [Manuscript File]

To view all the submission files, including those not included in the PDF, click on the manuscript title on your EVISE Homepage, then click 'Download zip file'.

Dear Editor,

Please find enclosed the manuscript: "**Photocatalytic, corrosion protection and adhesion properties of acrylic nanocomposite coating containing silane treated nano zinc oxide: a combined experimental and simulation study**", by Javadi et al., for publication in Progress in Organic Coatings. All co-authors have agreed on the content of the manuscript.

We believe that the findings of our work in this research are of prime interest and fit very well in the scope of Progress in Organic Coatings journal because they harness pivotal information on nanocomposite acrylic coating systems.

Thanks in advance for taking our paper into consideration and we shall appreciate your response at your earliest convenience.

Sincerely yours,

Dr. Mehdi Ghaffari
Golestan University,
Polymer Engineering Department, Faculty of Technology and Engineering
E-mail: M.ghaffari@gu.ac.ir
Tel: +98 17 32303988

Photocatalytic, corrosion protection and adhesion properties of acrylic nanocomposite coating containing silane treated nano zinc oxide: a combined experimental and simulation study

Ehsan Javadi[1], Mehdi Ghaffari[1,*], Ghasem Bahlakeh[2], Peyman Taheri[3]

[1] Department of Polymer Engineering, Faculty of Engineering, Golestan University, Gorgan, Iran.

[2] Department of Chemical Engineering, Faculty of Engineering, Golestan University, Aliabad Katoul, Iran.

[3] Delft University of Technology, Department of Materials Science and Engineering, Mekelweg 2, 2628 CD Delft, the Netherlands

Abstract

The influence of silane treated nano zinc oxide (nZnO) on the protection, photocatalytic properties and interfacial interactions in acrylic/carbon steel systems was investigated. For this purpose, nZnO particles have been synthesized using microwave irradiation method. The morphology of synthesized zinc oxide nanoparticles was studied by scanning electron microscopy (SEM). The nZnO were treated by 3(2-amino ethyl amino) propyl trimethoxysilane. Fourier transforms infrared spectroscopy (FTIR) and thermogravimetry (TGA) techniques have been used to prove success of nZnO surface treatment. In the next step, nanocomposites were prepared and coated on carbon steel by dip-coating method. Corrosion resistances of coatings were evaluated by electrochemical impedance spectroscopy (EIS). Field emission scanning electron microscopy (FE-SEM) has been carried out to study morphology of cross section of films. Moreover, to study the hydrophillicity and photocatalytic properties of coating surface, contact angle of the nanocomposites coating surface have been measured. Finally interfacial adhesion and their mechanisms have been studied by molecular dynamics (MD) and first principle quantum mechanics (QM) simulation method.

Keywords: Self-cleaning; Zinc oxide; Simulation; nanocomposite; surface treatment; acrylic.

1. Introduction

Photocatalysis and related research topics' popularity is growing while the technologies applied to natural remediation, clean chemical synthesis and solar energy conversion process[1] are currently areas which have a chance for improvement. Photocatalytic reactions occur when a particle absorbs a photon equal or more energetic than its band gap. In this situation, an electron from the valence band (VB) excited to conduction band (CB) creating a hole-electron pair. This hole-electron pair is able to start oxidation and reduction processes[2]. In order to have photocatalytic surfaces we need to use photocatalytic materials such as TiO_2, Fe_2O_3, WO_3 and ZnO. ZnO based on its unique properties such as high chemical stability[3], broad range of radiation absorption[4], biocompatibility, biodegradability[5] etc. is a good material to use in self-cleaning surfaces[6, 7], corrosion-resistant coatings[8-10], and electrostatic coatings[11].

The final properties of composite coatings are strongly dependent on the particle size, the quality extent of dispersion as well as particle/matrix interaction [12]. Reducing the particle size to the nano scale may lead to serious challenges to obtain homogenous dispersion. This can be attributed to the lack of affinity between the nano particle/polymer interfacial contact areas. Controlling the surface chemistry and functional groups by surface treatment is a critical issue for nanoparticles and their interactions [13]. Chen et al prepared nano zinc oxide then treated with aminopropyltriethoxysilane (APTS) and stearic acid, where they found that dispersion and long-term stability of modified ZnO in organic solvents were improved[14].

Utilization of organic coating on metal substrate is one of the common methods to corrosion protection of metals. Although organic coatings are an effective and economic solution, diffusion of corrosive agents and hydrolytic degradation are their main weakness, limiting the amount of time they can protect metals [15]. In order to address this issue, the addition of nano

particles such as TiO_2, Fe_2O_3 and ZnO into organic coating were considered[16]. Therefore, the addition of ZnO not only helps assist photocatalytic properties, but also improves the protective performance of coatings. Effect of zinc oxide on protective performance of coatings has been studied in many researches. Ye et al investigated the effect of nZnO on corrosion resistance of polyurethane [17]. They reported that nZnO improved the anti-corrosion properties of polyurethane coating for the stainless steel substrate. In another research Dhoke and et al studied the effect of nano-ZnO particles on the corrosion behavior of alkyd-based waterborne coatings [8]. They results showed that, with increase in the concentration of nano-ZnO there was an improvement in the corrosion resistance, UV resistance and mechanical properties of the alkyd-based coatings on mild steel substrate. The same results reported by Rashvand and Ranjbar for polyurethane-based waterborne coatings [18]. Kathalewar et al modified ZnO by cyclic carbonate functional trialkoxy silane and added into the polyurethane matrix [19]. They showed that the surface modification of ZnO caused to improvement in corrosion performance properties.

The aim of this work is to study the effect of silane as a surface modifier and an enhancer of properties in acrylic/treated ZnO nanocomposite. For this purpose nanoparticles were treated with Silane coupling agent. The modified nano zinc oxide was characterized by FTIR and TGA Techniques. Modified zinc oxide dispersed in acrylic resin made up the nanocomposite applied on carbon steel substrate. Subsequently the protection properties and photocatalytic activity were studied. To understand the experimental observation of the interaction of acrylic, melamine and nano zinc oxide, molecular dynamic simulation and mechanic quantum have been carried out subsequently.

2. Experimental

2.1. Materials

Zinc acetate, ammonia solution (25% w/w), were purchased from Chem. Lab. The acrylic resin was cured with melamine resin prepared from Alvan paint Co. and surface modifier, [3-(2-aminoethylamino) propyl] trimethoxysilane provided from Sigma Aldrich. Silane coupling agent with amine functional group (Figure 1) had been chosen as surface modifier. The amine functional groups can assist dispersion of nZnO in acrylic melamine system via interfacial interactions between hydroxyl and amine groups shown in figure 1. All materials were used without extra purification.

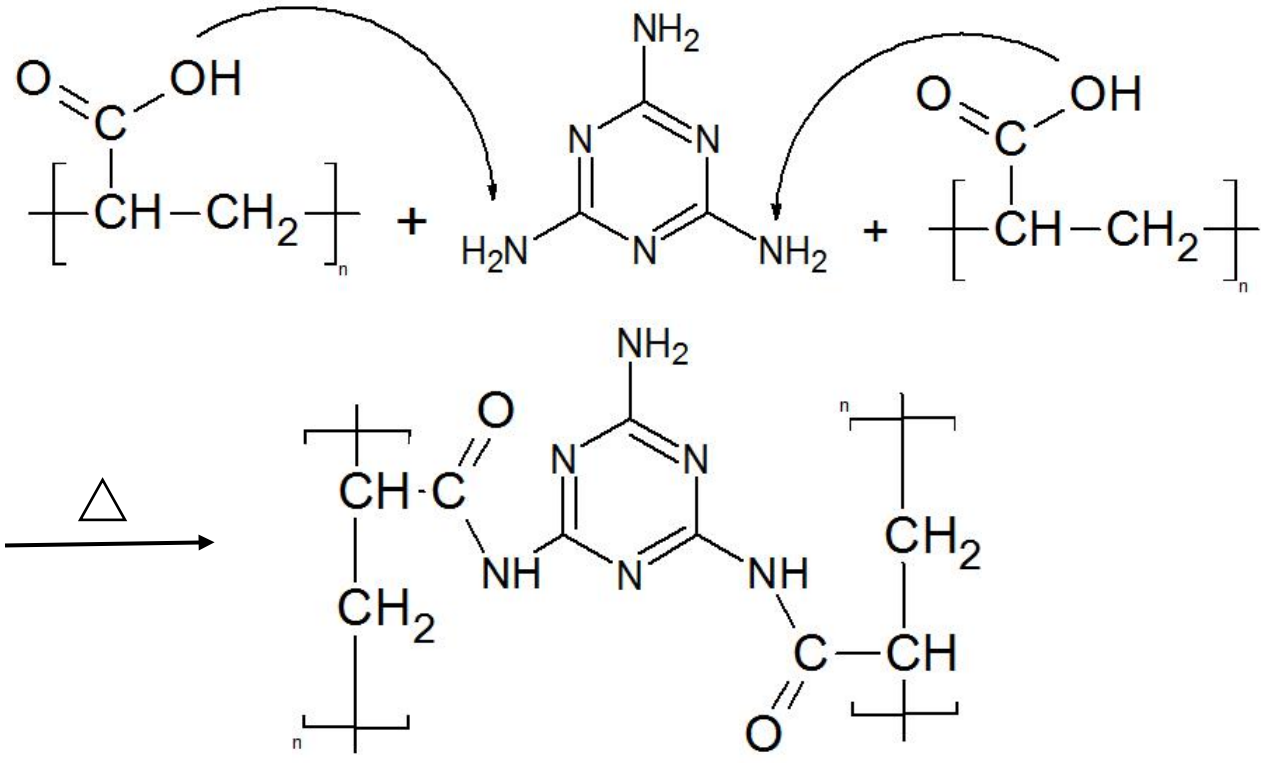

(a)

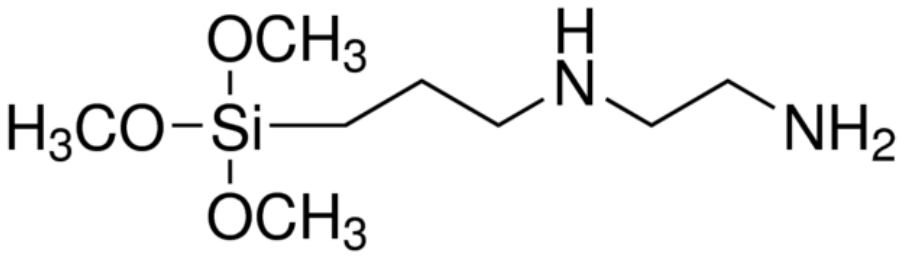

(b)

Figure 1. (a) Curing mechanism of acrylic acid by melamine and (b) Silane coupling agent: [3-(2-aminoethylamino) propyl] trimethoxysilane

2.2. Synthesis of ZnO

ZnO nano particles were prepared as follows: 10 ml of 1 mol.L^{-1} Zinc Acetate was mixed with 10 ml of ammonia and 230 ml distilled water. Next the solution was put in a microwave oven with 180 watts of power for 30 min. In the next step the obtained nano particles were filtered and washed three times with distilled water and finally dried for 24 hours at 50° C.

2.4. Modification of nano zinc oxide

For the surface modification of ZnO with silane coupling agent, 1 gr of ZnO nano particles were added to 100 ml distilled water, stirred 10 minutes and ultrasonicated 20 min. In the next step, the solution was stirred and heated until reaching 60° C. Afterwards, 1 ml silane was added drop wisely to the solution while it was stirred simultaneously. After 1 hour nano particles were washed and separated by centrifugation. Finally, modified nano ZnO was dried at 50°C for 4 hours in a vacuum oven.

2.5. Sample preparation

Nanocomposite acrylic coatings with different composition of modified ZnO (Table 1) were prepared by the following procedure: first treated nano zinc oxide was dispersed in solvent by 20

minutes sonication at room temperature. Then acrylic resin was added to the prepared solution and mixed with a mechanical stirrer to achieve homogeneous suspension and subjected to vacuum.

Table 1. Sample composition

Sample Name	ZnO (%)	Acrylic resin(gr)	Melamine resin(gr)	Solvent(gr)
NCZn.0	**0**	**27**	**12.5**	**30**
NCZn.0.3	**0.3**	**27**	**12.5**	**30**
NCZn.1	**1**	**27**	**12.5**	**30**
NCZn.5	**5**	**27**	**12.5**	**30**
NCZn.15	**15**	**27**	**12.5**	**30**

Subsequently melamine as an acrylic hardener was added and mixed thoroughly. Next, the prepared nanocomposites were coated on the surface of carbon steel by deep coating. The surfaces of carbon steel were abraded with abrasive papers of 80, 150, 220, 400, 500 and 1000 grit size. Finally prepared coatings were cured at 80 degrees C for 2 hours. The resulting thickness of the dried film thickness was 22 ±2 μm.

2.6. Experimental characterization

To study morphology of the synthesized nanoparticles and to prove the nanoscale dimension of particles in the coatings, field emission scanning electron microscopy was carried out using JEOL JSM-7000F FE-SEM. Fourier transforms infrared spectroscopy was performed by PEIR SPECTRUM ASCII PEDS1.60 in the 400-4000 cm^{-1} region to study the interactions between silane and ZnO. To investigate the heat stability, thermogravimetric analysis was done using Shimadzu TGA-50 (Japan) with 10°C/min heating rate in nitrogen atmosphere from room

temperature to 600°C. The photocatalytic activity was evaluated using an OCA15 plus-Dataphysics under UV light irradiation by the stearic acid method. The hydrophillicity behavior of nanocomposites was measured by contact angle of water droplets. The electrochemical impedance spectroscopy was done to study the anticorrosion performance of the nanocomposite system. The electrochemical measurements were carried out on an IVIUMSTAT-Vertex at open circuit potential (OCP) in 3.5 % NaCl aqueous solution within the frequency range of 0.01 to 100000 Hz.

2.7. Details of theoretical studies

2.7.1. Quantum mechanics calculations

In order to get electronic-level insight into our experimental observations quantum mechanics (QM) calculations were performed for methacrylic acid, melamine and 3-(2-aminoethylamino)propyltrimethoxysilane. These calculations were specifically carried out to examine the active sites of these molecules responsible for their adsorption onto metal oxide substrates. Figure 2 illustrates the molecular structure of methacrylic acid, melamine and trimethoxysilane. For QM calculations of these three molecules, first their geometries were optimized using Hartree-Fock (HF) theory applying the 6-31G(d,p) basis set [20]. The optimized geometries derived from HF calculation were then further refined by density functional theory (DFT) [21, 22] with the use of B3LYP functional for the computation of exchange-correlation interactions. DFT calculations were conducted initially with the 6-31G (d,p) basis function and then with a larger 6-311G (d,p) one [23-25]. All these HF and DFT computations performed using the Gaussian 09 package [26]. The methacrylic acid, melamine and rimethoxysilane structures with optimized geometries were then applied to determine the highest occupied molecular orbital (HOMO) and lowest unoccupied molecular orbitals (LUMO) as well as partial

charges. The average partial atomic charges were calculated by making use of ChelpG method [27].

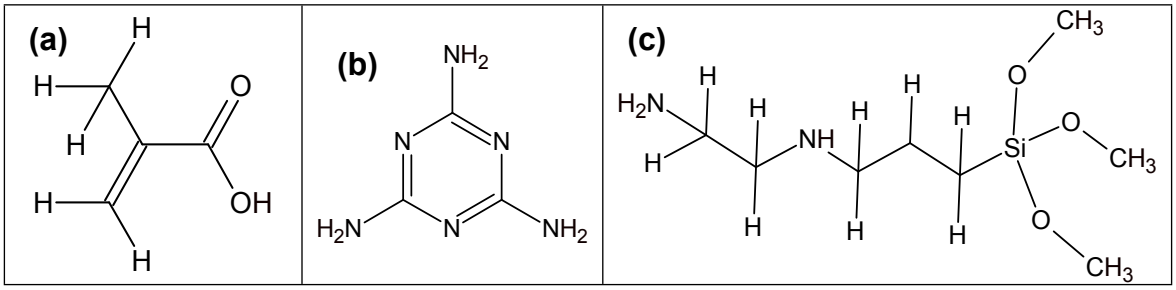

Figure 2. Molecular structures of (a) methacrylic acid, (b) melamine, and (c) 3-(2-aminoethylamino)propyltrimethoxysilane.

2.7.2. Construction of metallic substrates

After geometry optimization of methacrylic acid, melamine and trimethoxysilane using QM approaches the metallic substrates based on iron and zinc oxides were constructed. Three widespread forms of iron namely FeO (ferrous oxide), Fe_2O_3 (ferric oxide, hematite), and Fe_3O_4 (ferrous ferric oxide, magnetite) were used here to be representative of carbon steel substrates as employed in previous theoretical studies [28-32]. The interactions and adsorption properties of methacrylic acid, melamine and trimethoxysilane were examined with (100) and (110) crystalline surfaces in FeO & Fe_3O_4, and Fe_2O_3 respectively as these crystalline iron oxide surfaces proved the least lattice mismatch [33]. In case of zinc oxide (ZnO), the crystallographic plane ZnO (100) was chosen to assess the intermolecular interactions and adsorption properties of methacrylic acid, melamine hardener and trimethoxysilane. To build metal oxide substrates, first the surface builder module in Materials Studio software [34] was applied to cleave the corresponding crystalline unit cells of all three iron oxides and also zinc oxide along the aforementioned facets. The thickness of all cleaved surfaces was set to be about 1.5 nm. Subsequently, all metal oxide surfaces were periodically replicated along their surface directions.

To apply periodic boundary conditions along all three directions, a vacuum space of 3 nm was placed over the enlarged iron and zinc oxide surfaces.

2.7.3. Molecular dynamics simulations

To study the adsorption of methacrylic acid, melamine and trimethoxysilane over constructed iron and zinc oxide surfaces, their lowest energy geometries obtained from the last step of QM computations (i.e., DFT calculation at B3LYP/6-311G (d, p) level) were positioned over the FeO (100), Fe_2O_3 (110), and Fe_3O_4 (100), and also over the ZnO (100) substrates at larger distances from the surface. Then, all prepared simulation cells were optimized for 5000 steps with the use of Smart minimizer algorithm of For cite module available in Materials Studio software [34]. In the next step, the optimized cells were subjected to 500 ps MD simulations, which were performed in NVT ensemble at 298 K. During both static (i.e., optimization) and dynamics simulations all potential energy parameters except the partial atomic charges of methacrylic acid, melamine and trimethoxysilane molecules were taken from the COMPASS force field [35, 36]. The intermolecular interactions based on van der Waals (vdW) and columbic terms were modeled by atom-based cutoff and Ewald schemes, respectively. For the integration of Newton's equation the integrator of velocity, Verlet with 1 fs time step was utilized [37]. Also, within both optimization and MD simulation, the position of all metal oxide atoms namely, Fe, Zn and O was kept frozen at their bulk values.

3. Results and discussion

3.1. Morphology of synthesized zinc oxide

SEM micrographs of pure ZnO are shown in Figure 3. It can be seen that the morphology of the nano particles is mainly a mixture of rod and plates, while in some parts nano particles have agglomerated forming star morphology based on Figure 3, rod shaped particles are more

commonly seen. It seems that the dimension of rod shaped particles is within micrometer range whereas plate diameters are less than 100nm.

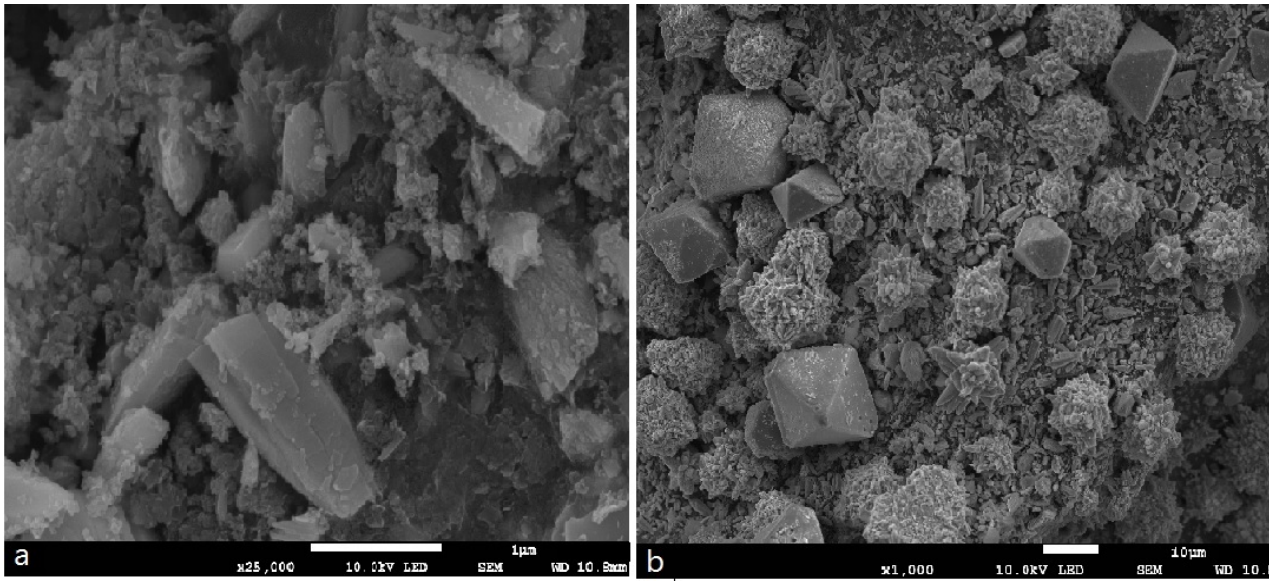

Figure 3. SEM images of nano ZnO

3.2. Experimental characterization of treated ZnO

3.2.1. Fourier transforms infrared spectroscopy (FTIR)

FTIR spectra of pure ZnO and modified ZnO have been showed in Figure 4. The peaks at 3235, 1627, 1080 and 715 cm^{-1} are related to the –OH stretching vibration, C=O stretching vibration of CO_2, C-N stretching vibration and N-H wag respectively [38, 39]. Farzi et al reported that absorption at 941 cm^{-1} is devoted to the Zn-O-Si stretching vibration[40], Hong [41] and Lihitkar [42] also confirmed these results. So it can be concluded that the peak at 921 cm^{-1} is related to Zn-O-Si and shows the formation of covalent bonds between ZnO and silane [43]. Also the absorption at 1035 cm^{-1} can be attributed to the untreated Si-O-CH_3. Thus the modification of ZnO by silane was successful based on the FT-IR results.

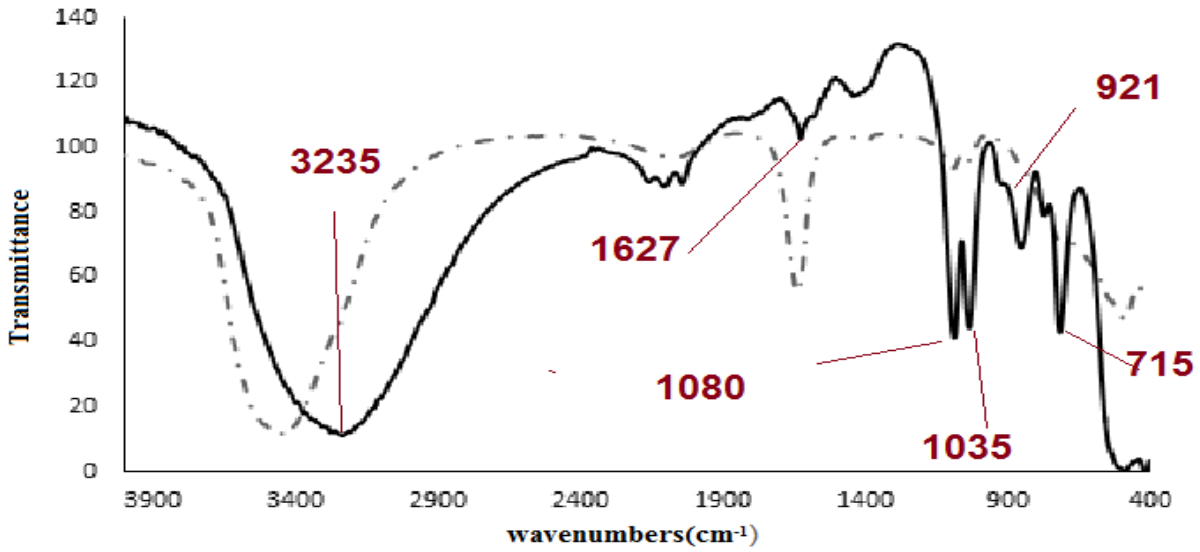

Figure 4. FTIR spectra of pure ZnO (Dash-Dot) and modified ZnO (solid)

3.2.2. Thermo gravimetric analysis

Figure 5 shows the TGA curves of pure ZnO and silane-grafted ZnO from room temperature to 600°C. It can be seen that in the range of 100 to 170°C, 3.79% weight of pure ZnO is lost. Degradation of contaminants or evaporation of water previously adsorbed onto the surface of pure ZnO can be the reason of this weight loss [44, 45]. Also shown in Figure 5 is the TGA curve of modified ZnO which shows 11.31% weight loss that can be related to the water evaporation and degradation of the silane grafted on the surface of ZnO. Thus about 8% of modified ZnO weight loss is related to the silane coated on the surface of ZnO.

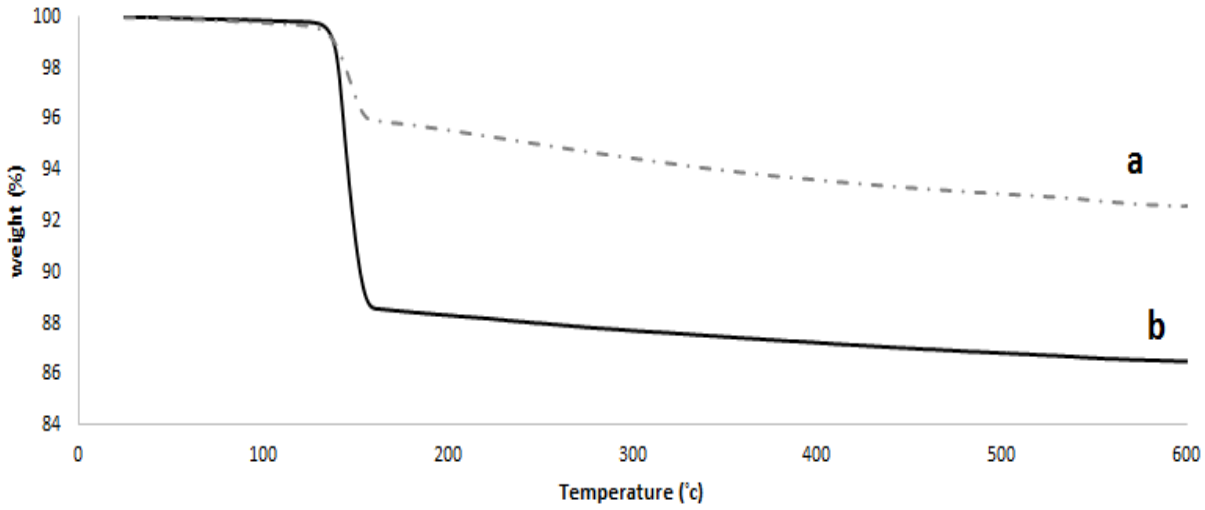

Figure 5. TGA curves of pure ZnO (a-Dash Dot) and silane-grafted ZnO (b-solid)

3.3. Electrochemical impedance spectroscopy (EIS)

Figure 6 shows the Bode, Nyquist and phase diagram of the samples after one day immersion in 3.5 % NaCl aqueous solution. The impedance value at low frequencies $|Z|_{0.01}$ is one parameter that is used to compare the protective performance of coatings. Figure 6.a shows that at low frequencies all of the samples have impedance values near 10^{10} Ω cm^2 after one day of immersion which shows high initial protective performance of coatings. Figure 7 shows a reduction of impedance value from 10^{10} to 10^8 Ω cm^2 for samples containing 5 and 15 percent of nZnO. Meanwhile, the phase angles shifted to higher frequencies for these samples which can attribute to formation of the pores in the coating due to agglomeration of nano zinc oxides and creating diffusion pass of electrolytes within the coating.

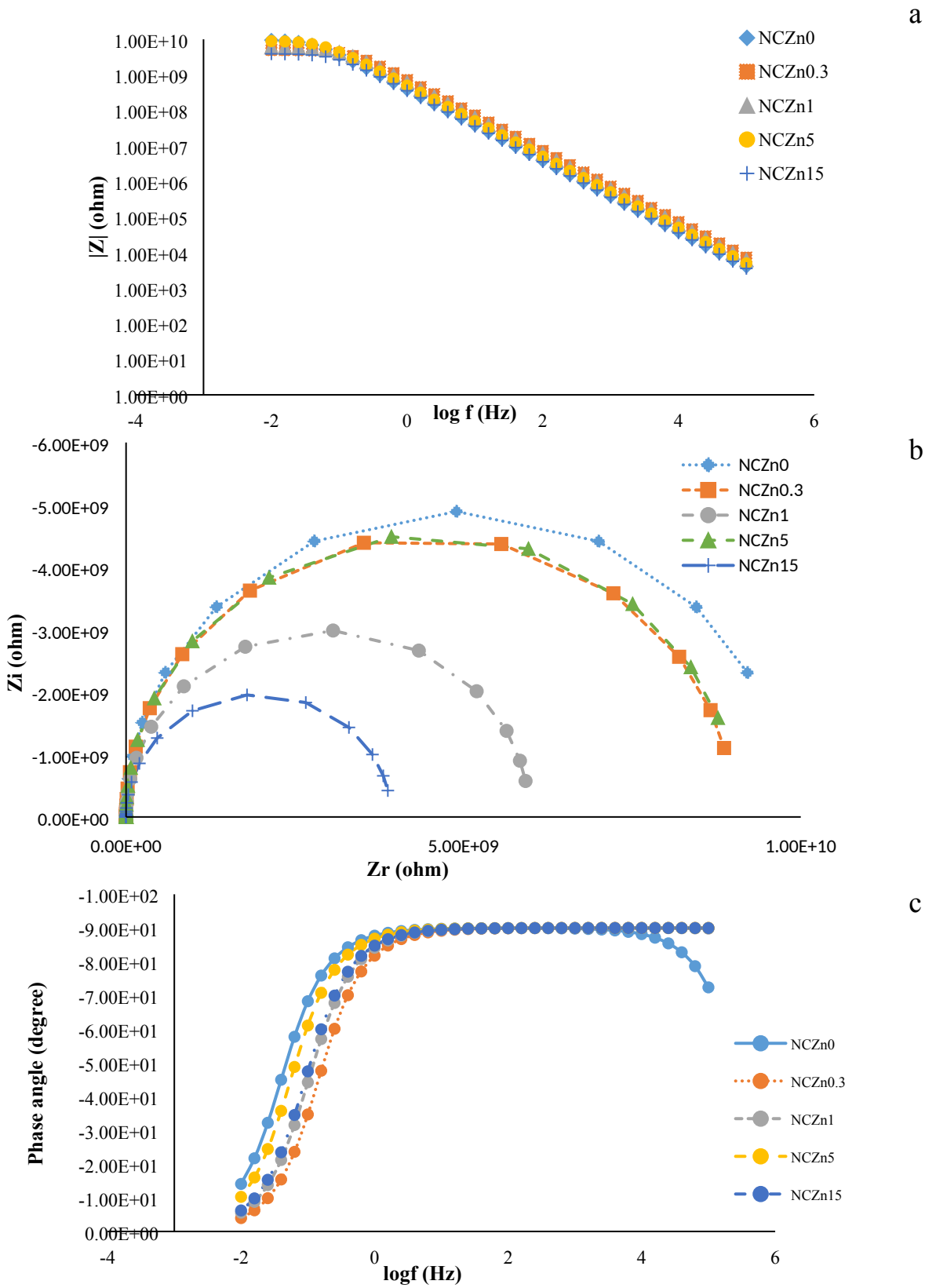

Figure 6. bode (a), Nyquist (b) and phase (c) diagrams of samples after one day immersion in 3.5 % NaCl aqueous solution

a

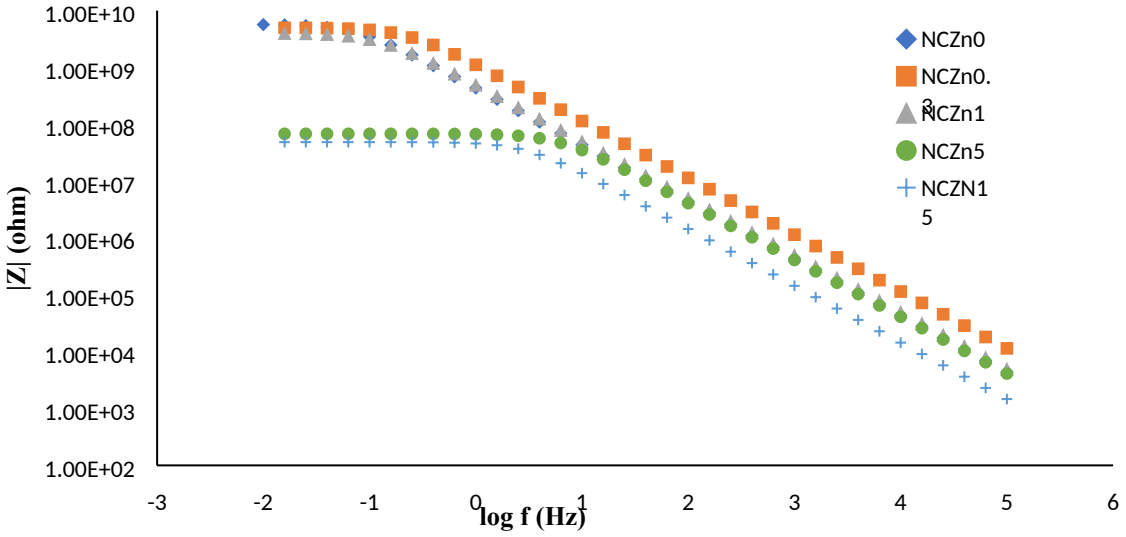
1.00E+10
1.00E+09
1.00E+08
1.00E+07
1.00E+06
1.00E+05
1.00E+04
1.00E+03
1.00E+02
|Z| (ohm)
-3
-2
-1
0
1
2
3
4
5
6
log f (Hz)
NCZn0
NCZn0.3
NCZn1
NCZn5
NCZN15

b

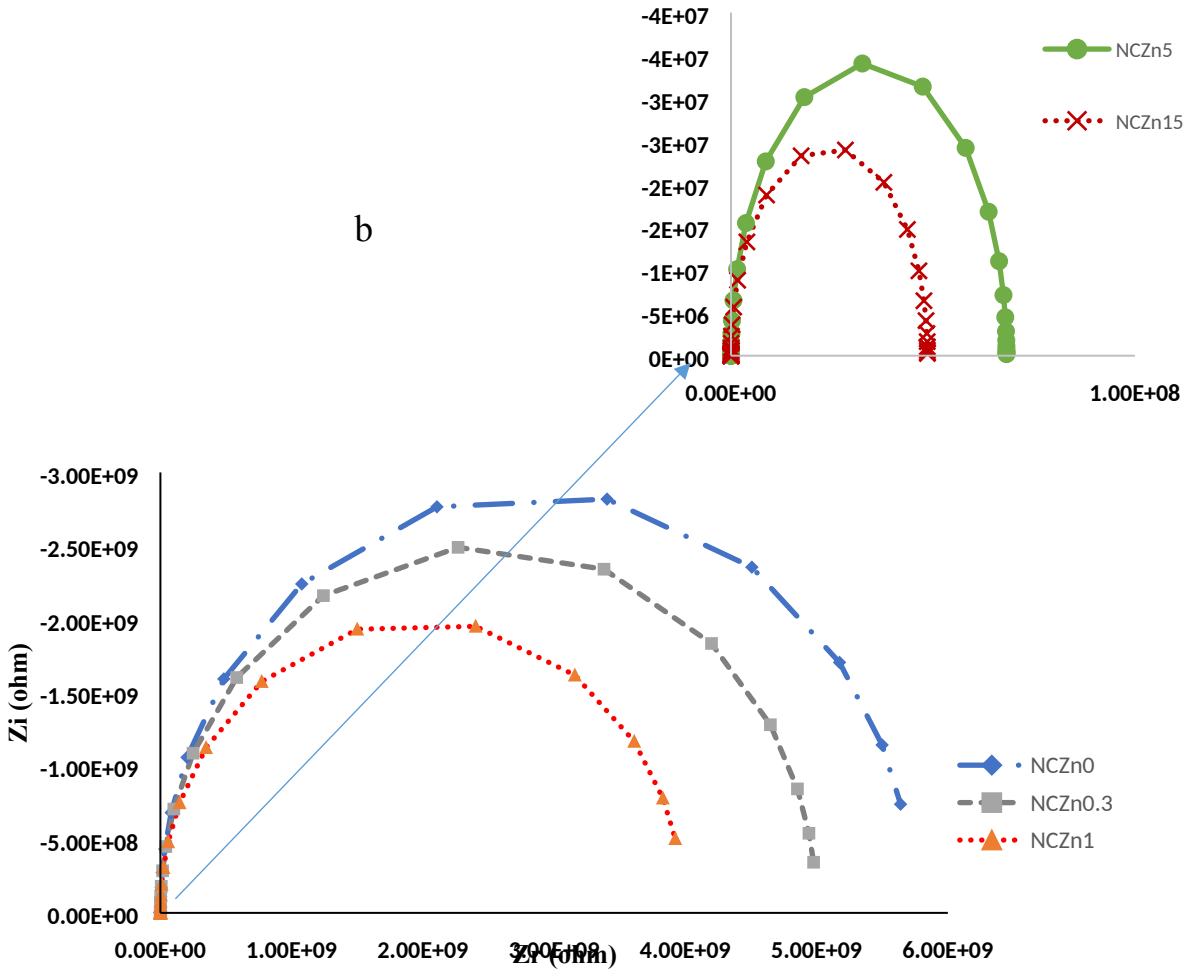
-4E+07
-4E+07
-3E+07
-3E+07
-2E+07
-2E+07
-1E+07
-5E+06
0E+00
0.00E+00
1.00E+08
NCZn5
NCZn15
-3.00E+09
-2.50E+09
-2.00E+09
-1.50E+09
-1.00E+09
-5.00E+08
0.00E+00
Zi (ohm)
0.00E+00
1.00E+09
2.00E+09
3.00E+09
4.00E+09
5.00E+09
6.00E+09
Zr (ohm)
NCZn0
NCZn0.3
NCZn1

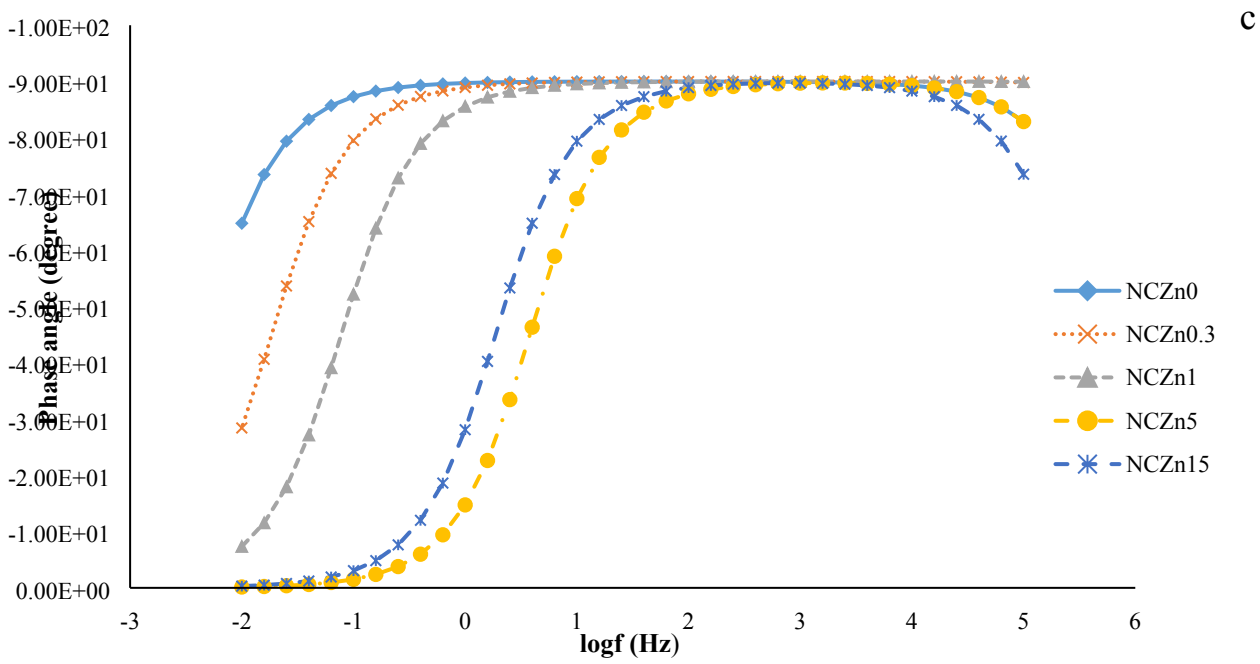

Figure 7. Bode (a), Nyquist (b) and phase (c) diagrams of samples after 15 days of immersion in 3.5 % NaCl aqueous solution

Figure 8 illustrates bode and Nyquist plots of samples after 1 month of immersion into 3.5 % NaCl aqueous solution. Due to continuous diffusion of electrolytes into the nanocomposite coatings impedance values in $|Z|_{0.01}$ reduced and impedance arcs became smaller as time continues. NCZn1 shows the highest impedance values which can be indicative of good dispersion of zinc oxide, which plays the role of physical barrier against the electrolyte penetration [9]. The sample NCZn15 displayed the lowest protection performance after 1 month immersion, which could be due to the tendency of nano zinc oxide particles to agglomeration in high concentration and the resulting formation of a pathway for corrosive agents to reach the metal surface[46].

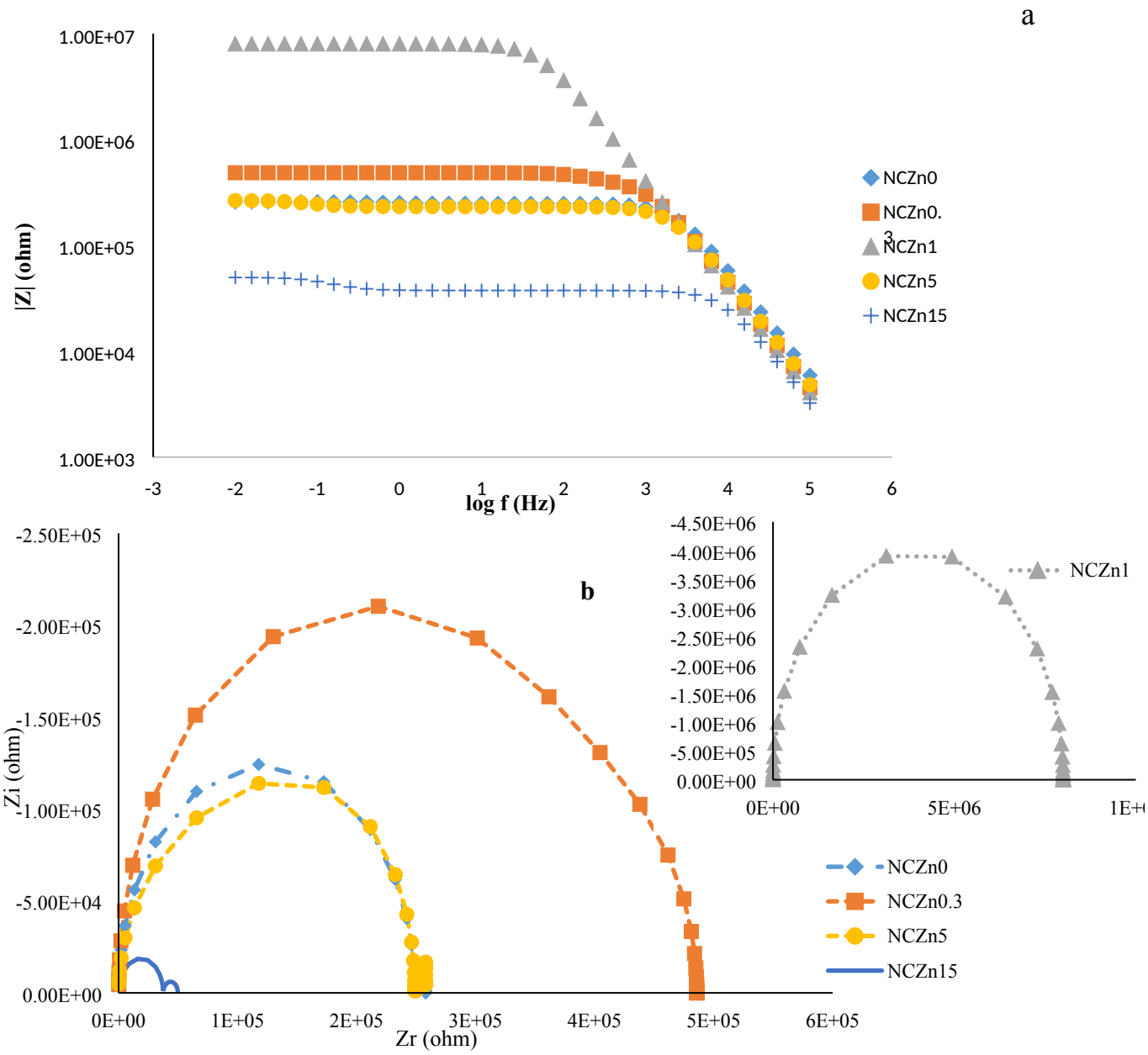
a
1.00E+07
1.00E+06
1.00E+05
1.00E+04
1.00E+03
|Z| (ohm)
-3
-2
-1
0
1
2
3
4
5
6
log f (Hz)
NCZn0
NCZn0.3
NCZn1
NCZn5
NCZn15
b
-2.50E+05
-2.00E+05
-1.50E+05
-1.00E+05
-5.00E+04
0.00E+00
Zi (ohm)
0E+00
1E+05
2E+05
3E+05
4E+05
5E+05
6E+05
Zr (ohm)
-4.50E+06
-4.00E+06
-3.50E+06
-3.00E+06
-2.50E+06
-2.00E+06
-1.50E+06
-1.00E+06
-5.00E+05
0.00E+00
0E+00
5E+06
NCZn1
NCZn0
NCZn0.3
NCZn5
NCZn15

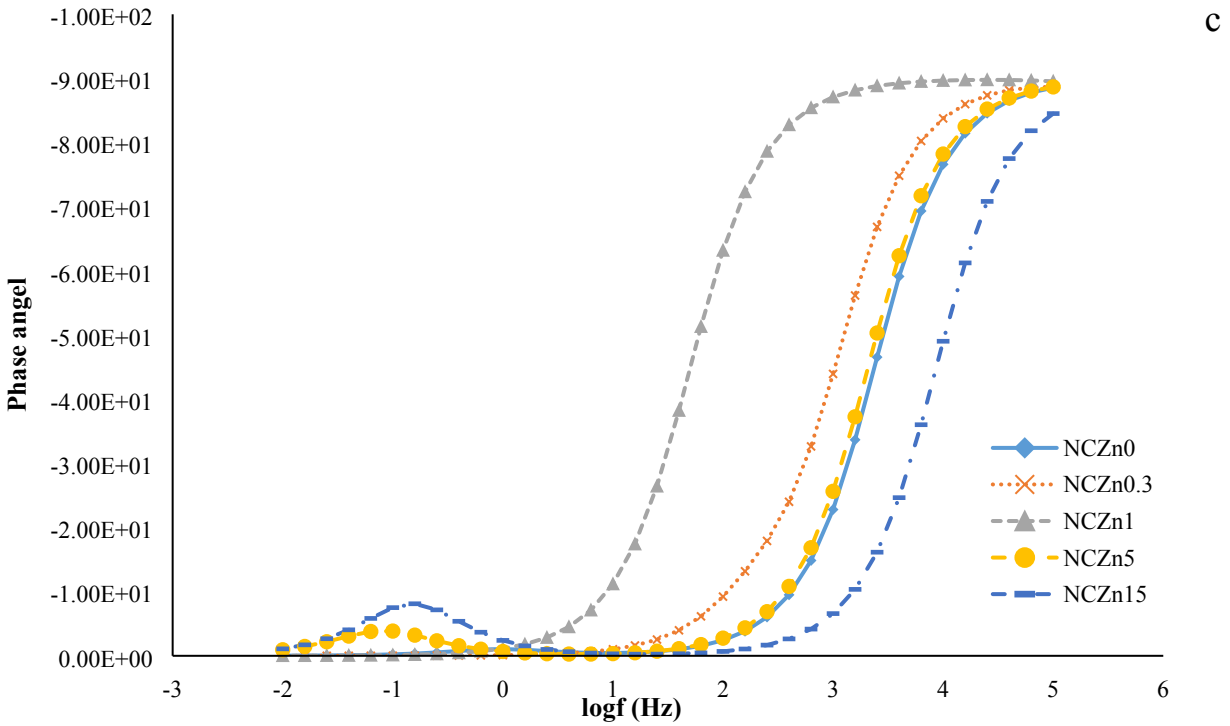

Figure 8. Bode (a), Nyquist (b) and phase (c) diagrams of samples after one month of immersion in 3.5 % NaCl aqueous solution

For further evaluation of protective performance of coating samples, EIS data were fitted with the electrical equivalent circuit shown in Figure 9. Since all Nyquist plots are characterized by two times constant within the whole exposure time, the equivalent circuit shown in Figure 9 has been used. In this model R_S represents solution resistance, Rct shows charge transfer resistance, R_C is coating resistance, C_C indicates coating capacitance and C_{dl} refers to double-layer capacitance at the substrate/electrolytes interface.

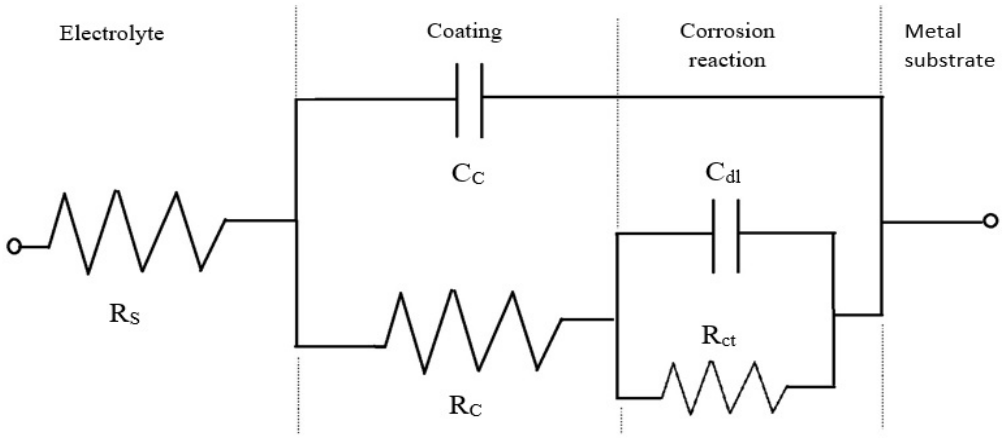

Figure 9. Equivalent circuits used to model EIS data

Variations with time of the different resistant parameters are shown in figure 10. The coating resistance extracted from impedance spectra (R_c) showed the coating permeability against the electrolyte. Time dependence decrease in coating resistance can be observed for all samples that can be attributed to the electrolyte penetration. For NCZn1, the Rc decreased at earlier exposure time to reach at almost constant value in prolonged immersion. Moreover, according to the results in figure 10-a, NCZn1 showed the highest coating resistant. The results for coating capacitance confirm the trend of coating resistance which NCZn1 and NCZn15 show highest and lowest barrier performance respectively.

According to the results, it can be concluded that samples show two behaviors within the whole exposure time: drop in the coating resistance and reach to approximately constant value. Decrease in coating resistance at early time can be due to the pore size while reach to constant value can be because of the blockage of the pores over long term exposure period. The second time constant of Nyquist plot represents the electro chemical reaction at the metal-coating interface. Hereupon, Cdl and Rct can be used as an indication of reaction initiation and loss of adhesion at metal-coating interface.

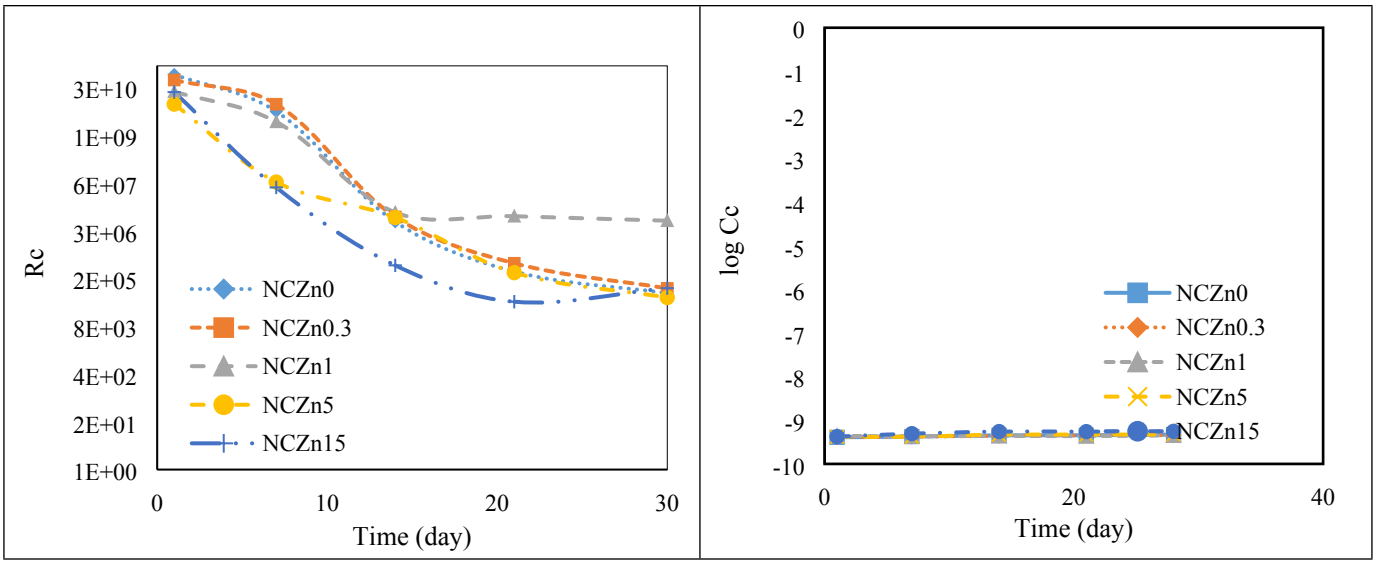

Figure 10. Effect of silane treated nano zinc oxide on R_C and C_c versus time.

Figure 11 shows Rct decrease during the immersion time for all the samples. NCZn15 decreased rapidly which is due to agglomeration of nanoparticles. The plots also illustrate the highest charge transfer resistance for NCZn1 during whole immersion time. The same behavior can be seen in double layer capacitance results as time elapses. It can prove that the NCZn1 has the best protection behavior within the immersion period.

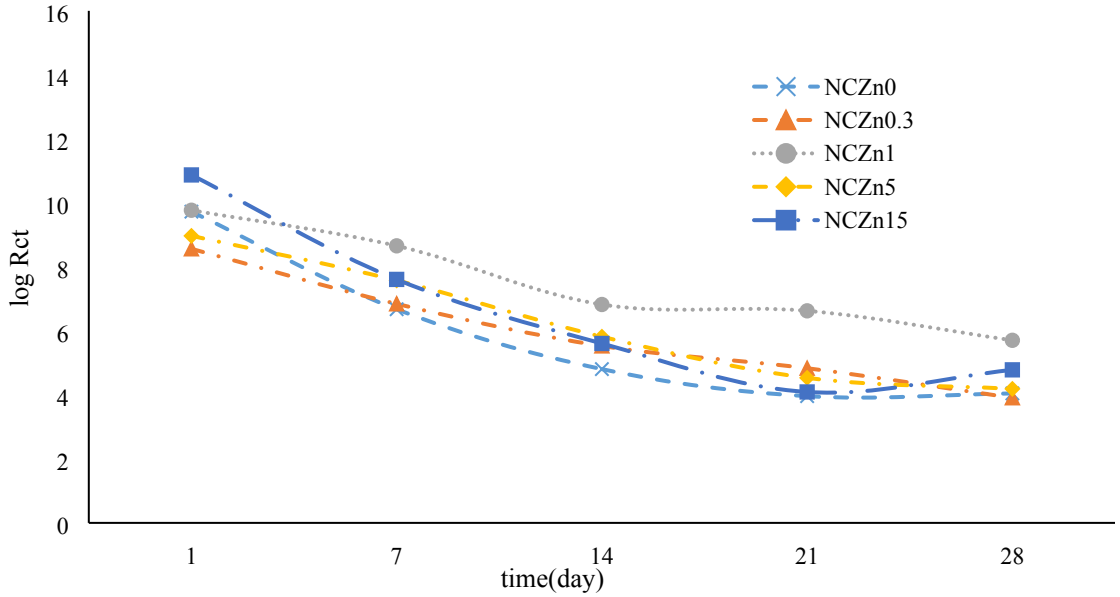

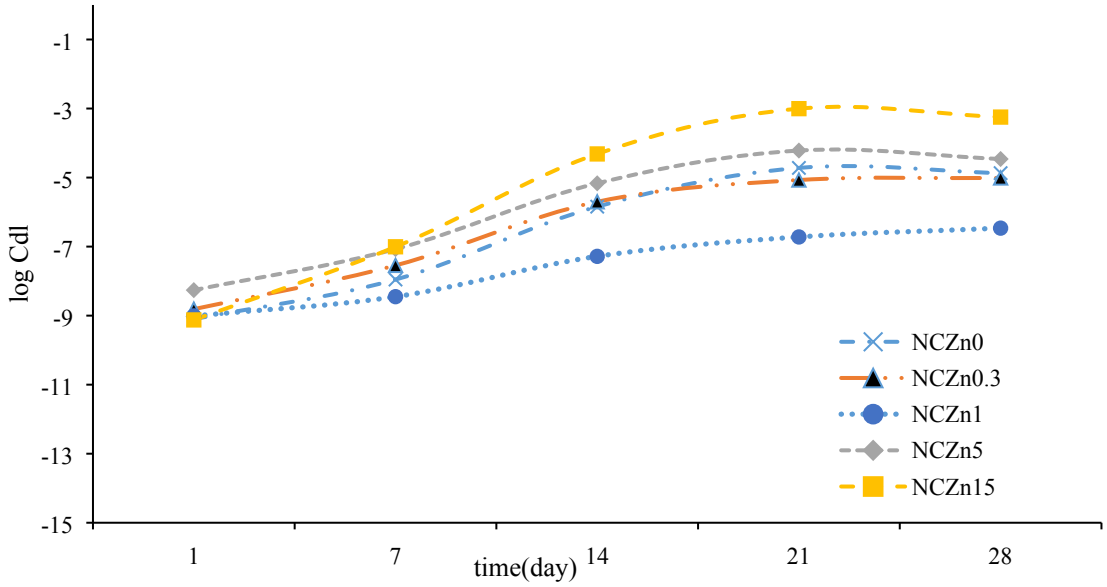

Figure 11. Effect of silane treated nano zinc oxide on Rct and Cdl

3.4. Morphology of the fractured surface of nanocomposite coating

To clarify the protection behavior of samples subjected within a corrosive environment the morphology of samples were studied. Also further analysis on dispersion extent of treated nano particles within the nanocomposites was carried out using the EDX-mapping images. FE-SEM micrographs of cross sections in Figure 12-a show almost a homogenous and smooth coating for NCZn1 sample. Figure 12-b shows that increasing ZnO content cause to formation of rough and bumpy surface as well as some pinholes in NCZn5 coating samples.

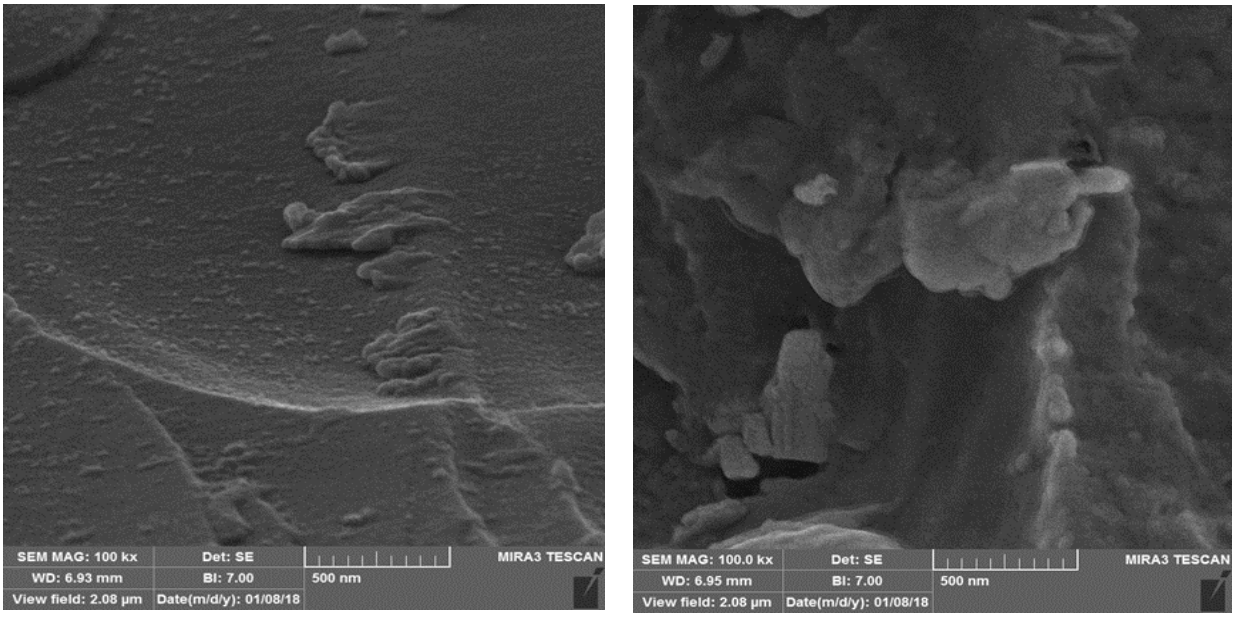

a b

Figure 12. FE-SEM images of a) NCZn1, and b) NCZn5

Figure 13 displays Zn mapping images for NCZn1 and NCZn5 Nanocomposites. Bright spots show Zn nanoparticles location, as expected NCZn1 illustrated a good dispersion with less agglomeration but NCZn5 shows in some parts nanoparticles accumulated that can create a pathway for electrolyte to penetrate into the coaching.

a

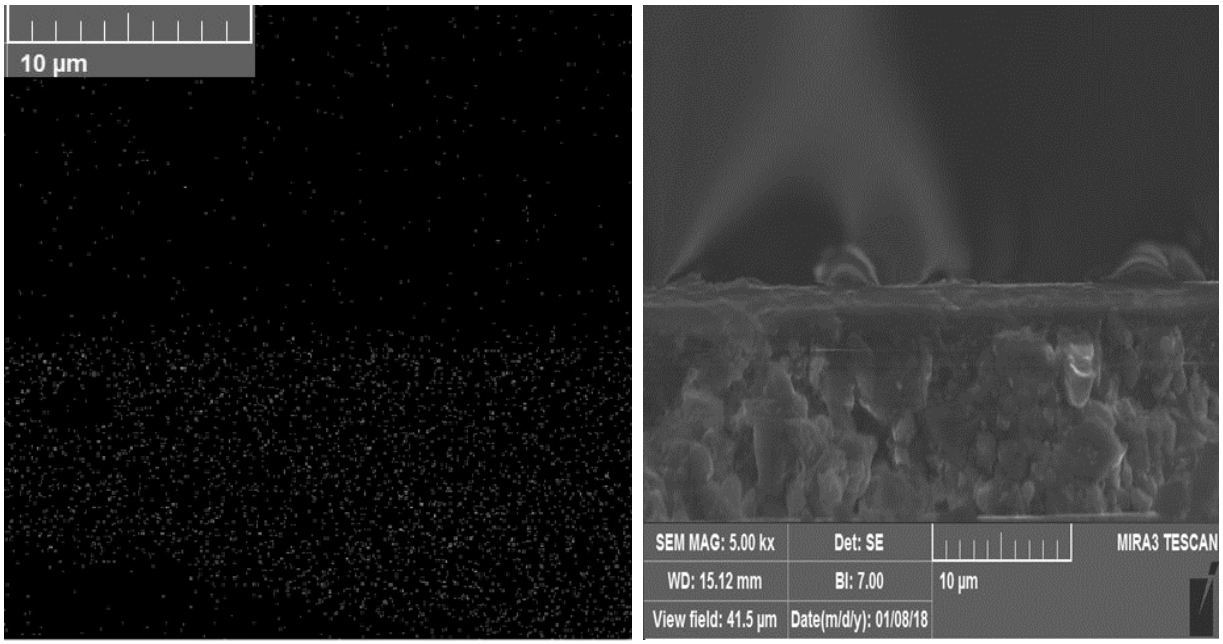

b

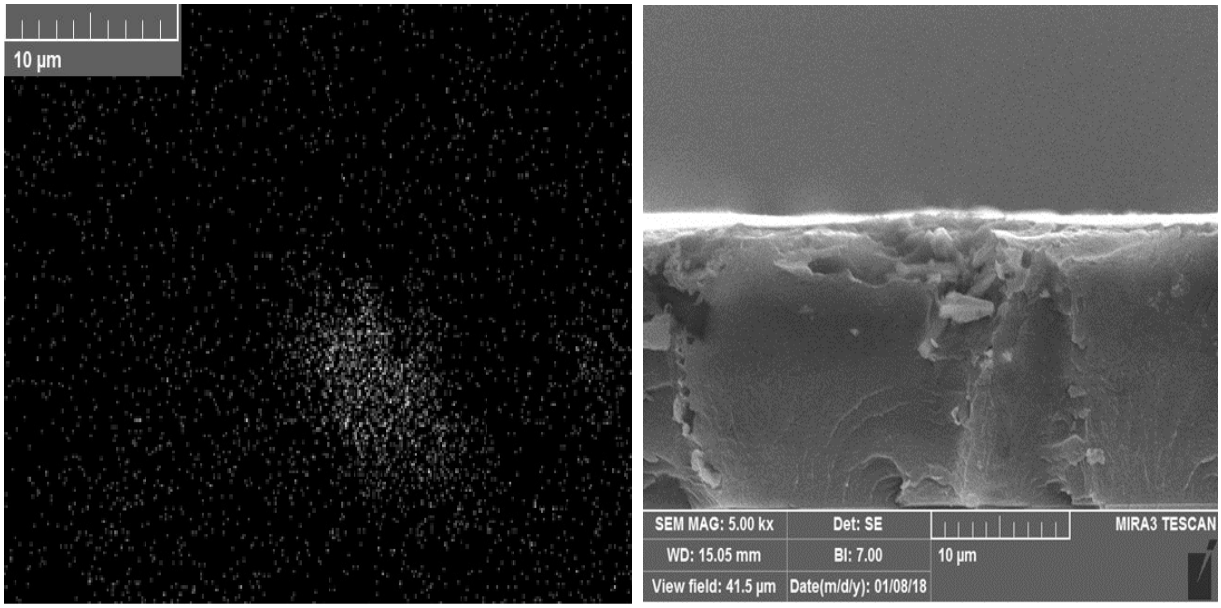

Figure 13. EDX-mapping images of a) NCZn1, and b) NCZn5

3.5. Contact angle

Contact angle is carried out to assess the hydrophillicity of samples. The contact angle of sample without nanoparticles has been obtained 84° that means the surface is relatively hydrophilic (figure 14). Based on the contact angle results, although NCZn0.3 had no significant changes in contact angle, but NCZn1 shows a drop in the contact angle which can be due to the more changes in surface chemistry of coatings as well as the roughness of coating surface in presence of 1% of nano zinc oxide [47, 48]. For two other samples, NCZn5 and NCZn15, no significant changes can be observed that can be because of the propensity of nano particles to aggregation at high quantities[49].

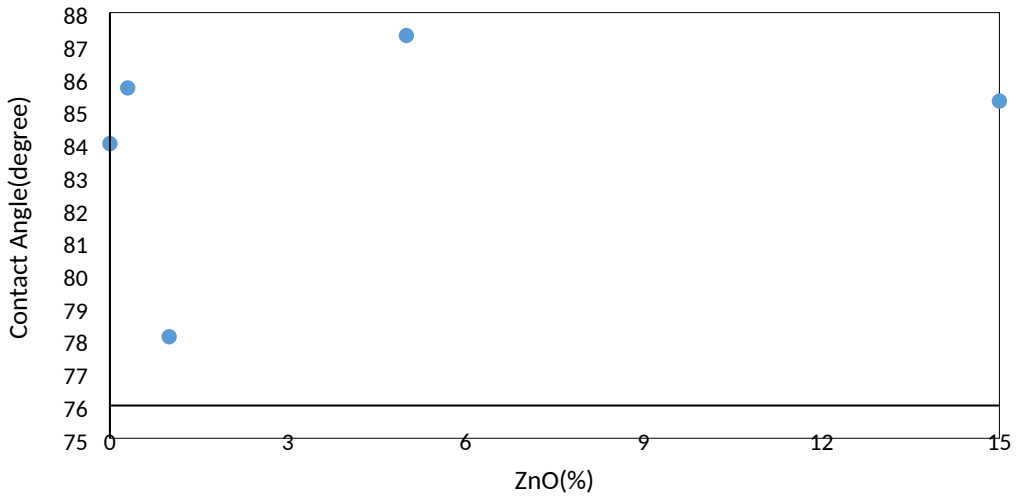

Figure 14. The contact angle of samples

3.6. Photocatalytic analysis

According to the previous results, it can be concluded that the nanocomposite sample containing 1% of nano zinc oxide showed the best results. So, to evaluate photocatalytic activity and self-cleaning performance, a thin layer of stearic acid coated on the surface of the NCZn1 and the contact angle measured at different times while the sample was under UV lights exposure. It was reported that in ZnO nanoparticles electrons excited from the valence band (VB) to conduction band (CB) and produce a hole-electron pair if they irradiated by UV light equal or more than its band gap [50]. Electrons in conduction band react with O_2 and produce peroxide radicals (figure 15). The aforementioned chemical reactions are:

$$e^- + O_2 \longrightarrow O^{\bullet}{}_2^-$$

$$O^{\bullet}{}_2^- + 2\,h^+ + e^- \longrightarrow H_2O_2$$

$$H_2O_2 + h^+ + e^- \longrightarrow OH^{\bullet} + H_2O$$

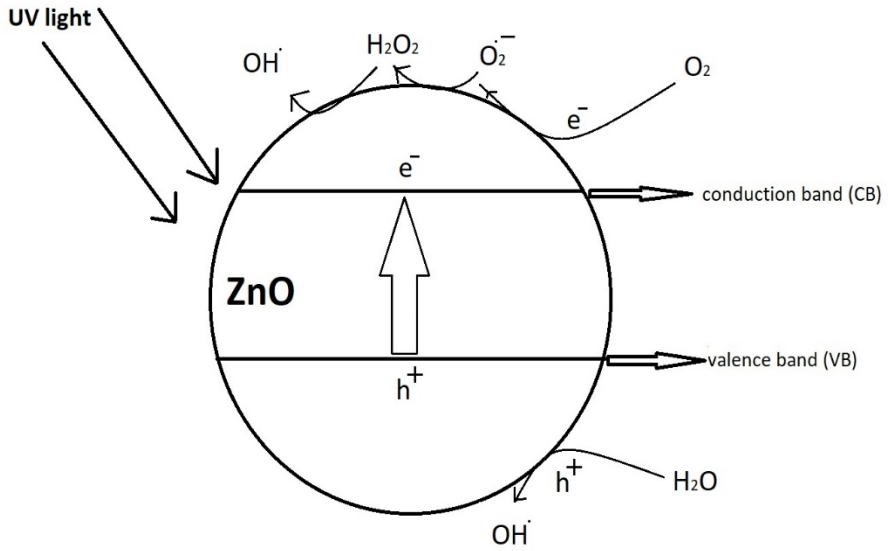

Figure 15. Schematic interpretation of the photocatalytic mechanism of ZnO

It can be seen that hole (h^+) react with H_2O and produce the $OH^{\bullet-}$ [50]. These peroxides can break the C-C and C-H bonds of pollution like stearic acid on the surface and leading to CO_2 and H_2O production [51]. So, degradation of stearic acid as pollution on the surface of nanocomposites leads to an increase in the degree of hydrophillicity. Figure 16 illustrated photocatalytic activity of NCZn1 as time elapse under UV exposure. Reduction in contact angle under UV irradiation confirmed the photocatalytic activity of NCZn1 on the surface of nanocomposites coatings which can degrade the surface pollution and clean the surface.

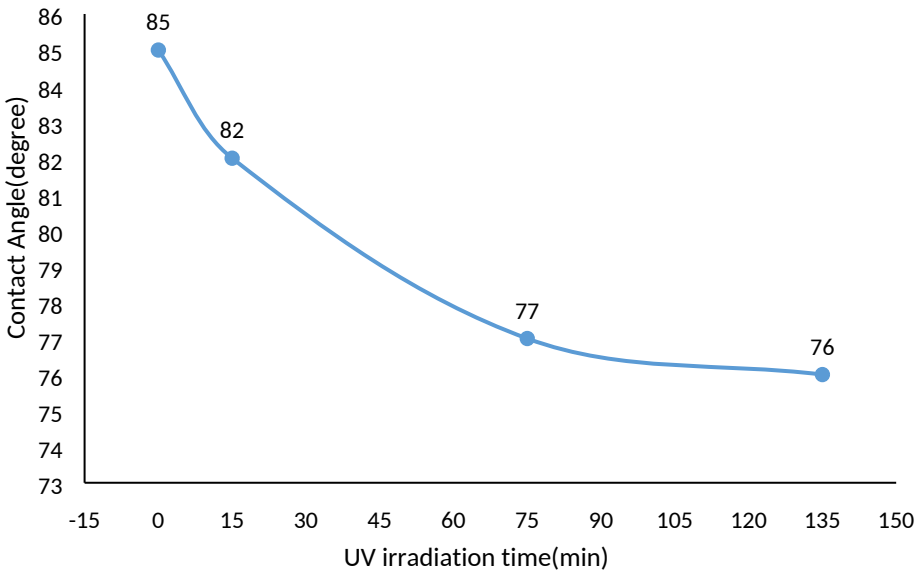

Figure 16. The photocatalytic activity of NCZn1 under UV exposure

3.7. MD simulation results

The constructed initial simulation cells along with final equilibrated structures of methacrylic acid, melamine and trimethoxysilane molecules interacted with iron oxides surfaces of FeO (100), Fe_2O_3 (110), and Fe_3O_4 (100) are displayed in Figure 17. Upon comparing the initial and final cells it is observed that distance of adsorbing molecules with the highest layer of all three iron oxides decreased. Such an observation suggests the affinity of methacrylic acid, melamine and trimethoxysilane to bind onto the chosen crystallographic surface of iron oxides representing the steel sheets. From the closer examination of the final visualized snapshots it can be seen that the oxygen atoms in methacrylic acid, nitrogen atoms of melamine and oxygen as well as nitrogen atoms of trimethoxysilane pointed towards the iron oxide substrates, especially Fe_2O_3 (110), and Fe_3O_4 (100) surfaces. Such a molecular alignment of surface-bound methacrylic acid, melamine and trimethoxysilane is related to the electrostatic interactions of the oxygen and nitrogen heteroatoms of these adhering molecules with iron atoms located at the uppermost layer of oxidized iron surfaces. The initial simulations along with the ultimate adsorbed configurations

of methacrylic acid, melamine and trimethoxysilane over the zinc oxide (ZnO) (100) substrate are depicted in Figure 18. The reduced distance of the adsorbate molecules from the outmost layer of zinc oxide in final snapshots in comparison with initial ones again declares the affinity of methacrylic acid, melamine curing agent and trimethoxysilane to attach onto the (100) plane within ZnO oxides crystals.

In order to quantitatively assess the adhesion of methacrylic acid, melamine curing agent and trimethoxysilane group with the chosen crystallographic surfaces of iron and zinc oxides, the adsorption energy (ΔE_{ads}) was computed using the expression of: $\Delta E_{ads} = E_{surface/adsorbate} - (E_{surface} + E_{adsorbate})$. In this formula, the term $E_{surface/adsorbate}$ is the potential energy of entire system (i.e., methacrylic acid, melamine or trimethoxysilane adsorbed to oxide surface), and $E_{surface}$ and $E_{adsorbate}$ are respectively indicative of the potential energies of the isolated metal oxide surface and isolated adsorbate molecule. The calculated adsorption energies of methacrylic acid, melamine and trimethoxysilane relevant for their ultimate cells shown in Figures 18 and 19 are summarized in Table 2. As listed in this table, it is noted that the adsorption energies of all three adsorbing molecules of methacrylic acid, melamine and trimethoxysilane over all three iron oxides and zinc oxide are negative, quantitatively implying the adhesion propensity of these adsorbate molecules onto steel substrates and also zinc oxide surfaces. According to the tabulated ΔE_{ads} data, it is seen that the adsorption energy of these three adsorbing molecules with Fe_2O_3 (110) surface is significantly higher than those of FeO (100) and Fe_3O_4 (100) surfaces. This observation declares the stronger binding of methacrylic acid, melamine and trimethoxysilane with Fe_2O_3 (110) as compared with the other oxidized iron surfaces, which is attributed to strengthened electrostatic interactions of O and N atoms with surface iron atoms of Fe_2O_3 oxide.

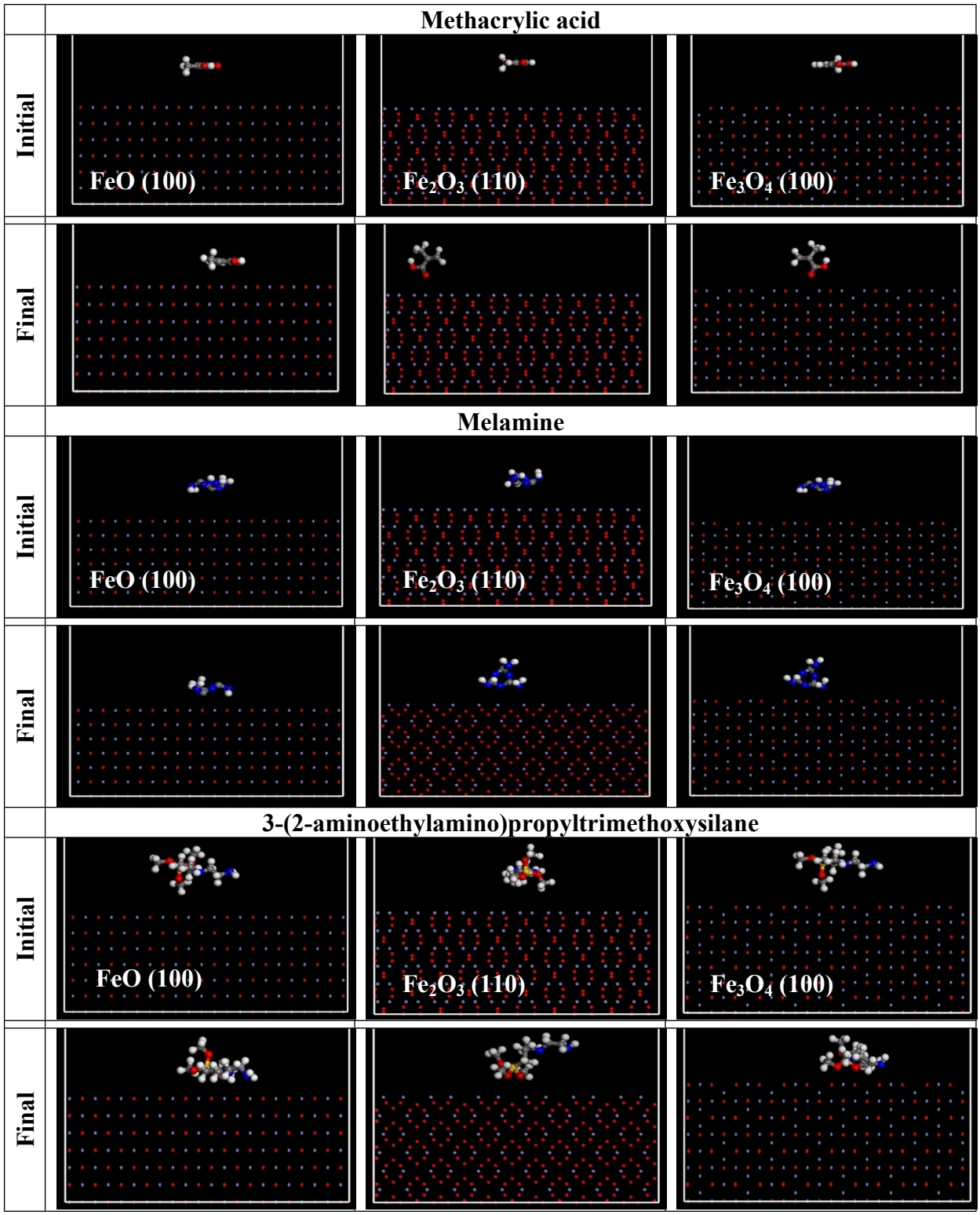

Figure 17. The initial and final structures of methacrylic acid, melamine and trimethoxysilane over FeO (100), Fe_2O_3 (110) and Fe_3O_4 (100) surfaces.

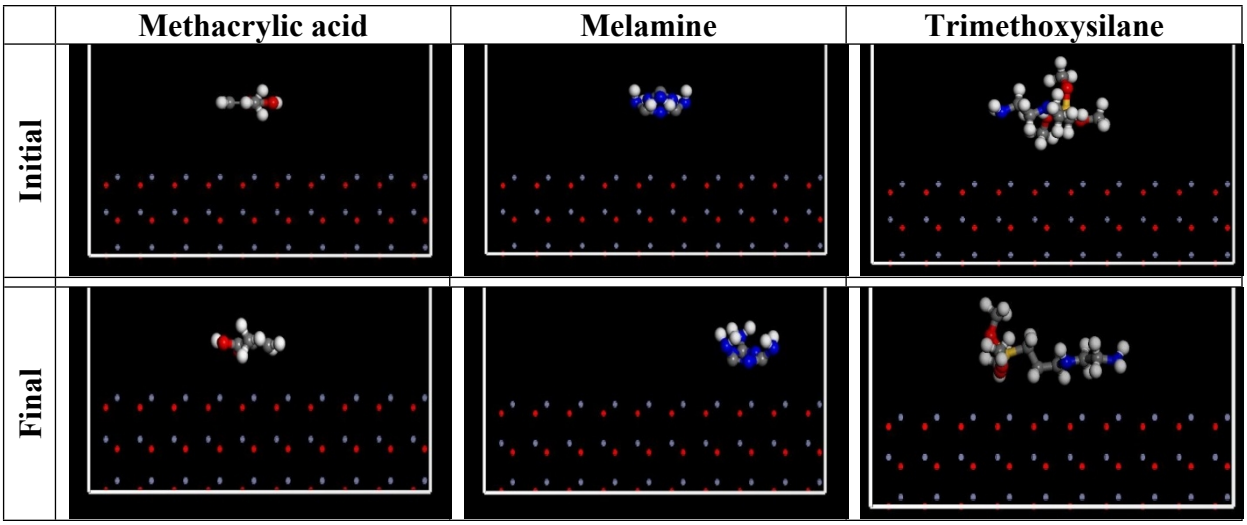

Figure 18. The initial and final structures of methacrylic acid, melamine and trimethoxysilane over ZnO (100) surfaces.

Table 2. The calculated interaction energies (kcal/mol) obtained at the end of MD simulations.

Material	Metal oxide surface (crystal plane)			
	FeO (100)	**Fe_2O_3 (110)**	**Fe_3O_4 (100)**	**ZnO (100)**
methacrylic acid	-16.67	-108.69	-75.34	-16.66
melamine	-24.18	-187.87	-115.04	-32.18
trimethoxysilane	-33.85	-220.86	-161.77	-44.56

3.8. QM computation results

To get electronic-level detail in regards to the interfacial interactions and active sites of methacrylic acid, melamine and trimethoxysilane affecting their adhesion behavior over the metal oxide substrates, the QM computations were carried out. From an electronic-level perspective, it is well-established that the interfacial adhesion of adsorbate molecule occurs via electronic donor-acceptor interactions [28, 31, 52-56]. In this adhesion mechanism, the active electron-rich groups of adhering molecule give their electrons in order to form the empty orbitals of metal cations. The ability of electron-rich sites to donate electrons to unfilled orbitals of surface atoms relies on their HOMO. On the other hand, the capacity of reactive centers of an

adsorbing molecule to accept electrons from the filled orbitals of surface metal atoms is dependent upon their LUMO distribution. Figure 18 illustrates the constructed images for optimized geometries as well as frontier orbitals (i.e., HOMO and LUMO) of methacrylic acid, melamine and trimethoxysilane extracted from the DFT/B3LYP/6-311G(d,p) level of theory. In case of methacrylic acid it is noted that the HOMO located on the carbonyl oxygen atom of carboxylic acid group and the carbon-carbon double bound, while its LUMO mostly distributed over the carbon atoms. As a consequence, the methacrylic acid could interact with oxidized surfaces through its electron-rich sites of carbonyl oxygen along with the C=C double bound. As shown, in the optimized melamine hardener the HOMO emerged on the whole aromatic ring as well as amine nitrogen atoms, and thus could involve in a donor-acceptor interaction with metallic surfaces via providing the delocalized π electrons of aromatic heterocycle and lone-pair electrons of amine N atoms to unoccupied orbitals of surface metal atoms. The carbon and nitrogen atoms of melamine also behaved as LUMO regions, an observation proposing their electron accepting tendency. Similarly, in case of optimized trimethoxysilane geometry it is noted that the HOMO almost appeared over the nitrogen atoms, implying electron sharing of trimethoxysilane though its nitrogen heteroatoms. On the other hand, the trimethoxysilane LUMO distributed on the silicon site and slightly on the methoxy oxygen atoms. Accordingly, the silicon atom of the trimethoxysilane could act as a main active site for accepting the electrons of occupied orbitals of surface Fe or Zn atoms.

To further examine the ability of methacrylic acid, melamine and trimethoxysilane in interfacial electrostatic and donor-acceptor interactions with oxidized substrates, the partial atomic charges distributed on the heteroatoms of these adsorbing molecules were computed and the results have been provided in Figure 19. It is apparent that the oxygen and nitrogen heteroatoms possessed

large negative charges. As a result, these active sites could have strong electrostatic interactions with surface metal cations and also share their electrons with unoccupied orbitals of surface atoms.

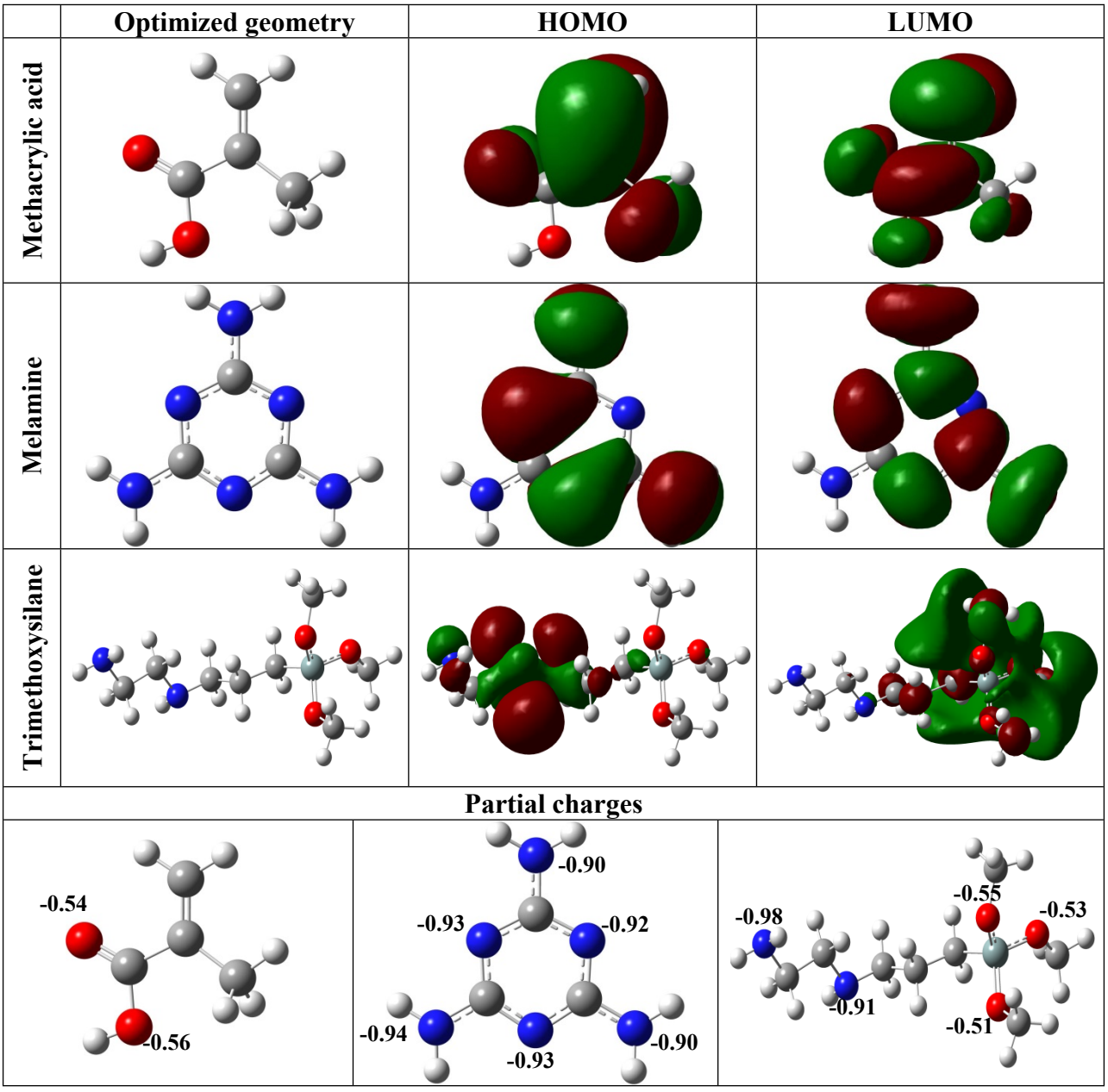

Figure 19. The optimized geometry, HOMO and LUMO of methacrylic acid, melamine and trimethoxysilane; Partial atomic charges of oxygen and nitrogen atoms in optimized geometries.

4. Conclusion

The nano zinc oxide particles were synthesized and modified by silane coupling agent. The results of TGA and FTIR prove the successful surface treatment of nZnO by silane. Acrylic/ treated ZnO nanocomposites were prepared and coated on carbon steel substrate. EIS results showed that presence of silane modified nano zinc oxide in acrylic coatings up to 1% wt. increased the protective performance of coatings. It can be due to the quality of dispersion of modified nZnO in acrylic matrix, as indicated by FE-SEM and EDX images. Moreover, the results of contact angle measurements displayed the highest hydrophillicity for nanocomposite containing 1% wt. of modified nano zinc oxide. Also, photocatalytic study showed that the contact angle of NCZn1 samples reduced by the irradiation time, which means that the coating surface has self-cleaning properties.

5. References:

1. Dionysiou, D.D., et al., *Photocatalysis: applications*. 2016: Royal Society of Chemistry.
2. Gouvea, C.A., et al., *Semiconductor-assisted photocatalytic degradation of reactive dyes in aqueous solution*. Chemosphere, 2000. **40**(4): p. 433-440.
3. Xu, J., Q. Pan, and Z. Tian, *Grain size control and gas sensing properties of ZnO gas sensor*. Sensors and Actuators B: Chemical, 2000. **66**(1-3): p. 277-279.
4. Kołodziejczak-Radzimska, A. and T. Jesionowski, *Zinc oxide—from synthesis to application: a review*. Materials, 2014. **7**(4): p. 2833-2881.
5. Zhou, J., N.S. Xu, and Z.L. Wang, *Dissolving behavior and stability of ZnO wires in biofluids: a study on biodegradability and biocompatibility of ZnO nanostructures*. Advanced Materials, 2006. **18**(18): p. 2432-2435.
6. Chae, D.W. and B.C. Kim, *Characterization on polystyrene/zinc oxide nanocomposites prepared from solution mixing*. Polymers for advanced technologies, 2005. **16**(11-12): p. 846-850.
7. Marci, G., et al., *Preparation characterization and photocatalytic activity of polycrystalline ZnO/TiO2 systems. 2. surface, bulk characterization, and 4-nitrophenol photodegradation in liquid− solid regime*. The Journal of Physical Chemistry B, 2001. **105**(5): p. 1033-1040.
8. Dhoke, S.K., A. Khanna, and T.J.M. Sinha, *Effect of nano-ZnO particles on the corrosion behavior of alkyd-based waterborne coatings*. Progress in Organic Coatings, 2009. **64**(4): p. 371-382.
9. Ramezanzadeh, B. and M. Attar, *Studying the corrosion resistance and hydrolytic degradation of an epoxy coating containing ZnO nanoparticles*. Materials Chemistry and Physics, 2011. **130**(3): p. 1208-1219.
10. Ghaffari, M. , et al., *Studying the effect of micro- and nano-sized ZnO particles on the curing kinetic of epoxy/polyaminoamide system*. Progress in Organic Coatings, 2015. **89**: P. 277-283.
11. Kitano, M. and M. Shiojiri, *Benard convection ZnO/resin lacquer coating—a new approach to electrostatic dissipative coating*. Powder Technology, 1997. **93**(3): p. 267-273.
12. Ghaffari, M. , et al., *Morphology, rheological and protective properties of epoxy/nano-glassflake systems*. Progress in Organic Coatings, 2014. **77**: P. 124-130.
13. Ghaffari, M., Naderi, R., and Ehsani, M., *Effect of silane as surface modifier and coupling agent on rheological and protective performance of epoxy/nano-glassflake coating systems*. Iranian Polymer Journal, 2014. **23**(7): p. 559-567.
14. Chen, H., Z. Guo, and L. Jia, *Preparation and surface modification of highly dispersed nano-ZnO with stearic acid activated by N, N′-carbonyldiimidazole*. Materials Letters, 2012. **82**: p. 167-170.
15. Pourhashem, S., et al., *Corrosion protection properties of novel epoxy nanocomposite coatings containing silane functionalized graphene quantum dots*. Journal of Alloys and Compounds, 2018. **731**: p. 1112-1118.
16. Tong, Y., S. Bohm, and M. Song, *The capability of graphene on improving the electrical conductivity and anti-corrosion properties of Polyurethane coatings*. Applied Surface Science, 2017. **424**: p. 72-81.
17. Ye, X. , et al., *Zinc oxide array/polyurethane nanocomposite coating: Fabrication,characterization and corrosion resistance*. Surface and Coatings Technology, 2019, **358**: P. 497-504.
18. Rashvand, M. and Ranjbar, Z., *Effect of nano-ZnO particles on the corrosion resistance of polyurethane-based waterborne coatings immersed in sodium chloride solution via EIS technique*. Progress in Organic Coatings, 2013, **76**: P. 1413-1417.
19. Kathalewar, M., Sabnis, A. and Waghoo, G., Effect of incorporation of surface treated zinc oxide on non-isocyanate polyurethane based nano-composite coatings. Progress in Organic Coatings, 2013, **76**:, P. 1215-1229.

20. Hariharan, P.C. and J.A. Pople, *The influence of polarization functions on molecular orbital hydrogenation energies*. Theoretica chimica acta, 1973. **28**(3): p. 213-222.
21. Hohenberg, P. and W. Kohn, *Inhomogeneous Electron Gas*. Physical Review, 1964. **136**(3B): p. B864-B871.
22. Kohn, W. and L.J. Sham, *Self-Consistent Equations Including Exchange and Correlation Effects*. Physical Review, 1965. **140**(4A): p. A1133-A1138.
23. Becke, A.D., *Density-functional thermochemistry. III. The role of exact exchange*. The Journal of Chemical Physics, 1993. **98**(7): p. 5648-5652.
24. Lee, C., W. Yang, and R.G. Parr, *Development of the Colle-Salvetti correlation-energy formula into a functional of the electron density*. Physical Review B, 1988. **37**(2): p. 785-789.
25. McLean, A.D. and G.S. Chandler, *Contracted Gaussian basis sets for molecular calculations. I. Second row atoms, Z=11–18*. The Journal of Chemical Physics, 1980. **72**(10): p. 5639-5648.
26. Frisch, M., et al., *Gaussian 09, revision D. 01*. 2009, Gaussian, Inc., Wallingford CT.
27. Breneman, C.M. and K.B. Wiberg, *Determining atom-centered monopoles from molecular electrostatic potentials. The need for high sampling density in formamide conformational analysis*. Journal of Computational Chemistry, 1990. **11**(3): p. 361-373.
28. Bahlakeh, G., et al., *A close-up of the effect of iron oxide type on the interfacial interaction between epoxy and carbon steel: combined molecular dynamics simulations and quantum mechanics*. The Journal of Physical Chemistry C, 2016. **120**(20): p. 11014-11026.
29. Bahlakeh, G., B. Ramezanzadeh, and M. Ramezanzadeh, *Cerium oxide nanoparticles influences on the binding and corrosion protection characteristics of a melamine-cured polyester resin on mild steel: An experimental, density functional theory and molecular dynamics simulation study*. Corrosion Science, 2017. **118**: p. 69-83.
30. Bahlakeh, G., et al., *Corrosion protection properties and interfacial adhesion mechanism of an epoxy/polyamide coating applied on the steel surface decorated with cerium oxide nanofilm: Complementary experimental, molecular dynamics (MD) and first principle quantum mechanics (QM) simulation methods*. Applied Surface Science, 2017. **419**: p. 650-669.
31. Bahlakeh, G. and B. Ramezanzadeh, *A Detailed Molecular Dynamics Simulation and Experimental Investigation on the Interfacial Bonding Mechanism of an Epoxy Adhesive on Carbon Steel Sheets Decorated with a Novel Cerium–Lanthanum Nanofilm*. ACS Applied Materials & Interfaces, 2017. **9**(20): p. 17536-17551.
32. Bahlakeh, G., B. Ramezanzadeh, and M. Ramezanzadeh, *Corrosion protective and adhesion properties of a melamine-cured polyester coating applied on steel substrate treated by a nanostructure cerium–lanthanum film*. Journal of the Taiwan Institute of Chemical Engineers.
33. Feng, L., H. Yang, and F. Wang, *Experimental and theoretical studies for corrosion inhibition of carbon steel by imidazoline derivative in 5% NaCl saturated Ca(OH)2 solution*. Electrochimica Acta, 2011. **58**: p. 427-436.
34. Accelrys Software Inc., S.D., 2009.
35. Sun, H., *COMPASS: an ab initio force-field optimized for condensed-phase applications overview with details on alkane and benzene compounds*. The Journal of Physical Chemistry B, 1998. **102**(38): p. 7338-7364.
36. Sun, H., P. Ren, and J. Fried, *The COMPASS force field: parameterization and validation for phosphazenes*. Computational and Theoretical Polymer Science, 1998. **8**(1-2): p. 229-246.
37. Swope, W.C., et al., *A computer simulation method for the calculation of equilibrium constants for the formation of physical clusters of molecules: Application to small water clusters*. The Journal of Chemical Physics, 1982. **76**(1): p. 637-649.

38. Parthasarathi, V. and G. Thilagavathi, *Synthesis and characterization of zinc oxide nanoparticle and its application on fabrics for microbe resistant defence clothing*. International Journal of Pharmacy and Pharmaceutical Sciences, 2011. **3**(4): p. 392-398.
39. Smith, B.C., *Infrared spectral interpretation: a systematic approach*. 1998: CRC press.
40. Farzi, G., R. Tayebee, and S. Naghibinasab, *Surface modification of ZnO nano-particles with Trimetoxyvinyl Silane and Oleic Acid and studying their dispersion in organic media*. International Journal of Nano Dimension, 2015. **6**(1): p. 67.
41. Hong, R., et al., *Synthesis, surface modification and photocatalytic property of ZnO nanoparticles*. Powder Technology, 2009. **189**(3): p. 426-432.
42. Lihitkar, P., et al., *Confinement of zinc oxide nanoparticles in ordered mesoporous silica MCM-41*. Materials Chemistry and Physics, 2012. **133**(2): p. 850-856.
43. Cao, Z., et al., *Synthesis and UV shielding properties of zinc oxide ultrafine particles modified with silica and trimethyl siloxane*. Colloids and Surfaces A: Physicochemical and Engineering Aspects, 2009. **340**(1): p. 161-167.
44. Hang, T.T.X., et al., *Effect of silane modified nano ZnO on UV degradation of polyurethane coatings*. Progress in Organic Coatings, 2015. **79**: p. 68-74.
45. Salahuddin, N.A., M. El-Kemary, and E.M. Ibrahim, *Synthesis and Characterization of ZnO Nanoparticles via Precipitation Method: Effect of Annealing Temperature on Particle Size*. Nanoscience and Nanotechnology, 2015. **5**(4): p. 82-88.
46. Shi, X., et al., *Effect of nanoparticles on the anticorrosion and mechanical properties of epoxy coating*. Surface and Coatings Technology, 2009. **204**(3): p. 237-245.
47. Su, C., et al., *Fabrication of an optically transparent super-hydrophobic surface via embedding nano-silica*. Applied Surface Science, 2006. **253**(5): p. 2633-2636.
48. Chau, T., et al., *A review of factors that affect contact angle and implications for flotation practice*. Advances in colloid and interface science, 2009. **150**(2): p. 106-115.
49. Ammar, S., et al., *Amelioration of anticorrosion and hydrophobic properties of epoxy/PDMS composite coatings containing nano ZnO particles*. Progress in Organic Coatings, 2016. **92**: p. 54-65.
50. Lu, M., *Photocatalysis and water purification: from fundamentals to recent applications*. 2013: John Wiley & Sons.
51. Ali, A.M., et al., *Preparation and characterization of ZnO–SiO2 thin films as highly efficient photocatalyst*. Journal of Photochemistry and Photobiology A: Chemistry, 2014. **275**: p. 37-46.
52. Khaled, K., *Studies of iron corrosion inhibition using chemical, electrochemical and computer simulation techniques*. Electrochimica Acta, 2010. **55**(22): p. 6523-6532.
53. Musa, A.Y., R.T. Jalgham, and A.B. Mohamad, *Molecular dynamic and quantum chemical calculations for phthalazine derivatives as corrosion inhibitors of mild steel in 1M HCl*. Corrosion Science, 2012. **56**: p. 176-183.
54. Zhang, J., et al., *Theoretical evaluation of corrosion inhibition performance of imidazoline compounds with different hydrophilic groups*. Corrosion Science, 2011. **53**(1): p. 147-152.
55. John, S., M. Kuruvilla, and A. Joseph, *Adsorption and inhibition effect of methyl carbamate on copper metal in 1 N HNO3: an experimental and theoretical study*. RSC Advances, 2013. **3**(23): p. 8929-8938.
56. John, S., et al., *Electrochemical, quantum chemical, and molecular dynamics studies on the interaction of 4-amino-4H, 3, 5-di (methoxy)-1, 2, 4-triazole (ATD), BATD, and DBATD on copper metal in 1N H2SO4*. Materials and Corrosion, 2011. **62**(11): p. 1031-1041.